Electronic Supplementary Material (ESI) for RSC Advances.

Supplementary Information

Mononuclear Nickel(II)-Flavonolate Complexes of Tetradentate Tripodal 4N Ligands as Structural and Functional Models for Quercetin 2,4-dioxygenase: Structures, Spectra, Redox and Dioxygenase Activity

Tamilarasan Ajaykamal,[a] and Mallayan Palaniandavar[a]*

[a]*Department of Chemistry, Bharathidasan University, Tiruchirapalli 620 024, Tamil Nadu, India*

Supplementary Information

Computed Structures

A Density Functional Theory (DFT) study has been performed at the computational level of U-B3LYP/6-31G* exchange correlation functional on the Ni(II)-flavonolate complexes **1**–**3** to throw light on their unique structural features and stabilities and also to illustrate their reactivity towards dioxygen. The initial coordinates of **1** and **3** were taken from their single crystal X-ray structures and the calculated structures subjected to optimization. And the computed structural parameters of the optimized geometries (**Table 2**, **Fig. 2**) are in close agreement with those of the X-ray structures. Thus, the calculated Ni–N1 (**1**, 2.095; **3**, 2.084), Ni–N2 (**1**, 2.149; **3**, 2.260), Ni–N3 (**1**, 2.060; **3**, 2.063), and Ni–N4 bond lengths (**1**, 2.095; **3**, 2.087) are close to the experimental values. However, the calculated Ni–$O1_{hydroxylate}$ bond lengths (**1**, 2.044; **3**, 2.049 Å) are longer than the experimental bond lengths (**1**, 1.984(4); **3**, 1.962(5) Å) while the calculated Ni–$O2_{carbonyl}$ bond lengths (**1**, 2.113; **3**, 2.119 Å) are close to or slightly longer than the experimental bond lengths (**1**, 2.110(4); **3**, 2.144(6) Å). The calculated bond angles are close to the octahedral bond angles of 90° and 180°. So, the calculated structures and the structural parameters are valid and may be used to discuss the trends in bonding and reactivities. The small differences in the observed and computed bond parameters may be because the computations are performed in CH_3CN as solvent medium. Also, we have calculated the structures of the other geometric isomer **1b**–**3b** (**Fig. 2**) for both the S = 0 and S = 1 spin states and the latter has energies lower than the former, as revealed by the three ligand field bands observed for the complexes (cf. below). In these octahedral structures the fla^- possesses an orientation different from that in **1**–**3**. It may be noted that the X-ray structures of both the geometric isomers of $[Ni(Me_3TACN)(fla)]^+$ have been reported.[1]

The computed molecular structure of **1** is similar to its X-ray structure with the octahedral NiN_4O_2 chromophore being constituted by the pyridyl N3 (Ni–N3, 2.060 Å, **Table 1**) and amine N2 (Ni–N2, 2.149 Å) nitrogens of **L1** ligand and O1 (Ni–O1, 2.044 Å) and O2 (Ni–O2, 2.113 Å) atoms of flavonolate and the N1 (Ni–N1, 2.095 Å) and N4 (Ni–N4, 2.095 Å) pyridyl nitrogens of **L1** coordinated trans to each other at equal bond lengths. The calculated asymmetry (Δd) in fla^- binding is 0.069 Å while the observed value is 0.126 Å (cf. above). The computed structure of **2** is distorted octahedral, similar to that of **1**. Interestingly, the two 6-Me-pyridyl nitrogens N1 and N4 are located trans to each other at almost the same bond lengths (Ni–N1, 2.216; Ni–N4,

2.222). The Ni–N1, Ni–N4 and Ni–N2 bonds in **2** are longer than the corresponding Ni–N bonds in **1**, obviously due to steric hindrance of 6-Me group to coordination of pyridyl nitrogen; however, the Ni–N3 bond lengths are the same. The Ni–O1 bond in **2** (2.051 Å) is longer and the Ni–O2 bond is shorter (2.099 Å) than the respective Ni–O bonds in **1** (Ni–O1, 2.044; Ni–O2, 2.113 Å), with the asymmetry in coordination of flavonolate anion in **2** being lower than that in **1** (Δd: **1**, 0.069 Å; **2**, 0.048 Å). Thus, the incorporation of sterically hindering 6-methyl substituent on pyridyl ring decreases the electron density on Ni(II), resulting in weaker π-back bonding of (2)C=O bond and hence the lower π-delocalization in fla$^-$ of **2**. However, there is no change observed in (2)C=O (**1**, 1.297; **2**, 1.297 Å), C1–C2 (**1**, 1.471; **2**, 1.467 Å), and C1–O1 (**1**, 1.342; **2**, 1.343 Å) bond lengths.

The calculated energies of HOMO and SOMOs (HOMO-1, HOMO-2/6) of all the four complexes are collected in **Table 2** (**Fig. S3**, **S4**). Interestingly, the doubly filled HOMO is localized on the coordinated fla$^-$, and is higher in energy than the SOMOs.[1] This non-Aufbau electronic configuration is expected of π-conjugated molecules like H(fla), conferring enhanced stabilities on them, and such HOMO-1–HOMO inversions have been observed previously (Ref 65). It may be noted that the HOMO-1 and HOMO-2 are made up of $d_{x^2-y^2}$ (σ*) and d_z2 (σ*) orbitals respectively of Ni(II). The HOMO is a highly conjugated π-MO of fla$^-$ while the LUMO is the unoccupied highly conjugated π* orbital. The observed trend in HOMO energy, H(fla) (-6.002) < **2** (-5.613) < **1** (-5.582) < **3** (-5.508 eV), is the same as that in LUMO energy, **2**(-2.567) < **1** (-2.526) < **3** (-2.480 eV), and a plot of the values of the two energies is linear, reflecting that the 4N ligands influence the π-delocalization in fla$^-$ and hence its dioxygenation. The calculated HOMO-LUMO energy gap (**Table 2**, **Fig**. **3**) varies as, **1** (3.056) > **2** (3.045) > **3** (3.029 eV), which corresponds to the observed band maxima, **1** (441) ~ **2** (441) > **3** (446 nm), cf. below) of the π→π* transition in Ni(II)-bound fla$^-$. The trend in HOMO energy reflects that the replacement of pyridyl nitrogen donor in **1** by the more basic bzim nitrogen donor to obtain **3** enhances the π-back bonding of Ni(II) with fla$^-$ enhances the π-delocalization and hence the asymmetry in fla$^-$ (Δd(exptl): **1**, 0.126; **3**, 0.182Å; cf. above), and raises the energies of both HOMO (π) and LUMO (π*). Interestingly, the inclusion of sterically hindering 6-Me group on **1** to obtain **2** lowers the π-delocalization, decreases the energies of both LUMO and HOMO and hence the asymmetry in fla$^-$ (Δd(calc): **1**, 0.067; **2**, 0.048Å). Accordingly, HOMO-1 ($d_{x^2-y^2}$) and

HOMO–2 (d_{z^2}) of **1** are inverted in **2**. It is expected that the higher the energy of HOMO the easier is the removal of electron from HOMO and hence more facile is the oxidation of fla^{-}.

In complexes **1** and **3**, the $d_{x^2-y^2}$ orbital is oriented towards N1N2N3O2 donor set while the d_{z^2} orbital is oriented towards N3O2 donor atoms. On the other hand, in **2**, interestingly, the d_{z^2} orbital is oriented towards N2O1 donors while the $d_{x^2-y^2}$ orbital is oriented towards N1N3N4O1 donor set. The orientation of d_{z^2} orbital towards N3O2 donor atoms for **1** and **3** is in accordance with the highest value of $T' = \frac{(\sum axial\ bonds)/2}{(\sum equatorial\ bonds)/4}$ calculated (**1**, 1.012; **3**, 1.003; **Table 2**) while the T′ values are lower for the alternative orientations towards N2N4 (**1**, 1.009; **3**, 0.993) and N2O1 (**1**, 0.979; **3**, 1.003). We have already shown that for octahedral Mn(II) complexes with $t_{2g}^3e_g^2$ configuration, the degeneracy of e_g orbitals is lifted up and whether d_{z^2} or $d_{x^2-y^2}$ forms the higher energy HOMO–1 orbital is determined by the value of T' and that the separation between the two orbitals vary in energy. However, for the computed structures, the T′ values (**Table 2**) predict that d_{z^2} prefers N2O1 for **1** and **3**, but actually it prefers N3O2 donors. Similarly, d_{z^2} in **2** should prefer to orient along N1N4 donors, but it is found to be oriented towards N2O1. Such inconsistencies may be traced to the computations performed in CH_3CN as solvent.

Table S1. Structure refinement details for **1** and **3**.

	1	**3**
Sum formula	C_{33} H_{27} Cl N_4 Ni O_9	C_{45} H_{42} Cl N_7 Ni O_7
Formula weight	717.74	887.01
Temperature (K)	296(2)	296(2)
Wavelength (Å)	0.71073	0.71073
Crystal system	triclinic	triclinic
Space group	P-1	P-1
a(Å)	8.7410(18)	10.101(5)
b(Å)	11.275(3)	14.304(7)
c(Å)	18.489(4)	15.831(8)
α(°)	79.476(15)	97.26(3)
β(°)	79.222(13)	96.87(3)
γ(°)	68.785(14)	109.19(3)
Volume (Å3)	1655.6(6)	2110.9(19)
Z	2	2
D_x (g.cm^{-3})	1.440	1.396
Reflections collected	8610	10823
R indices (all data)	0.0875, wR_2 =0.3004	0.1307, wR_2 =0.3920

Table S2. Selected bond angles [°] for **1** and **3**.

Bond angles/°	**1**	**3**
N1–Ni–N2	80.38(2)	78.57(2)
N1–Ni–N3	93.19(17)	89.06(3)
N1–Ni–N4	162.13(2)	156.14(3)
N1–Ni–O1	95.58(19)	105.01(2)
N1–Ni–O2	91.72(16)	89.26(2)
N2–Ni–N3	82.80(19)	80.93(3)
N2–Ni–N4	82.11(2)	78.76(2)
N2–Ni–O1	175.88(18)	175.72(2)
N2–Ni–O2	97.52(17)	100.89(2)
N3–Ni–N4	88.14(18)	94.62(3)
N3–Ni–O1	98.27(17)	96.68(2)
N3–Ni–O2	175.06(16)	177.23(2)
N4–Ni–O1	101.87(2)	97.97(2)
N4–Ni–O2	87.03(18)	87.81(3)
O1–Ni–O2	81.76(15)	81.64(2)

CCDC: 2039217 for complex [Ni(L1)(fla)](ClO_4) **1**

CCDC: 1956984 for complex [Ni(L3)(fla)](ClO_4) **3**

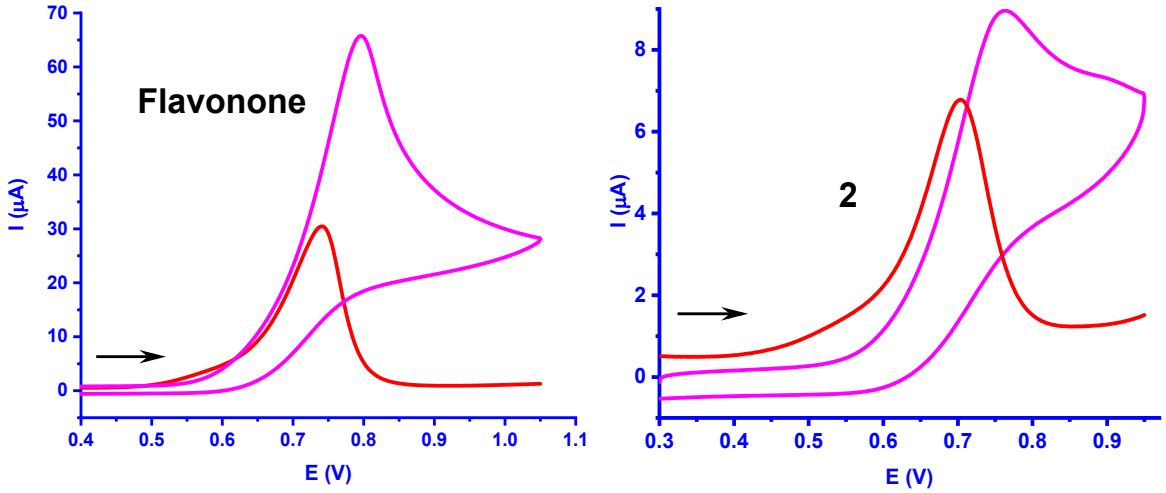

Figure S1. Cyclic voltammograms and DPV of flavonone ligand (1.0×10^{-3} M) and complex **2** in DMF at 25 ºC. Conditions: supporting electrolyte, 0.1 M TBAP; Scan rate, CV, 50 mVs^{-1} and DPV, 2 mVs^{-1} for all complexes, reference electrode, Calomel electrode; working electrode, Glassy carbon; Counter electrode, platinum wire.

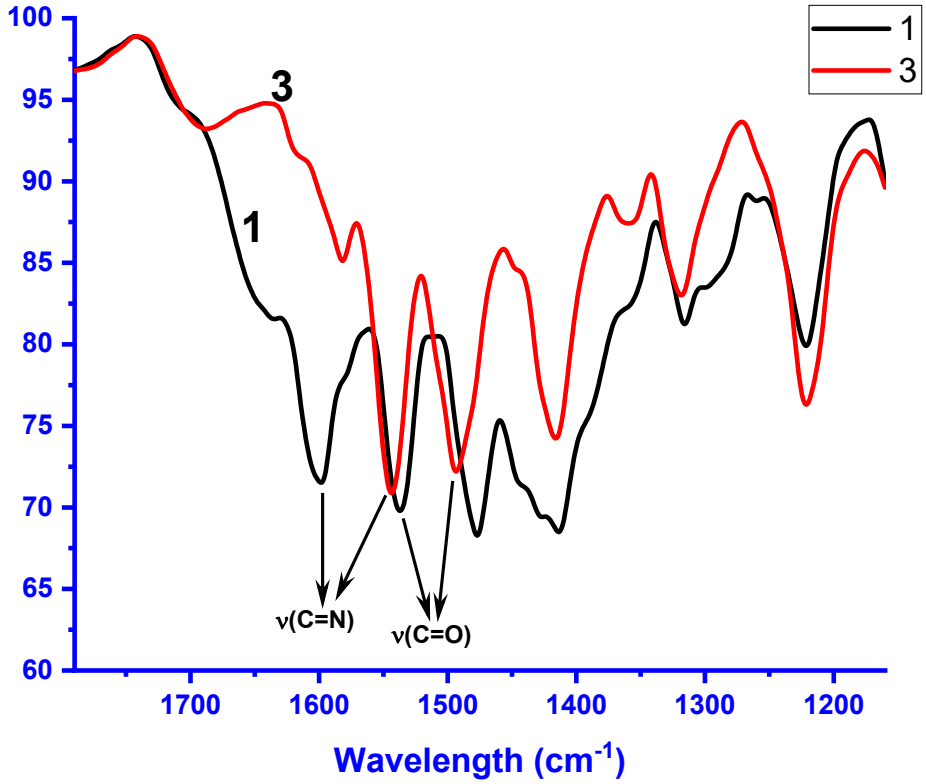

Figure S2. IR spectra of complexes **1** and **3**.

Table S3. Computed structural parameters and energy gap values of the geometric isomers **1b–3b**

Bond lengths/Å	**1b**		**2b**		**3b**	
	***HS**	**#LS**	***HS**	**#LS**	***HS**	**#LS**
Ni1–N1	2.102	1.934	2.220	1.998	2.092	1.929
Ni1–N2	2.151	2.453	2.118	2.388	2.265	2.643
Ni1–N3	2.069	1.939	2.071	1.945	2.056	1.912
Ni1–N4	2.102	1.935	2.220	1.991	2.092	1.927
Ni–O1	2.049	2.395	2.058	2.657	2.054	2.428
Ni1–O2	2.041	1.896	2.036	1.902	2.048	1.896
O1–C1	1.344	1.294	1.343	1.286	1.289	1.289
O2–C2	1.311	1.357	1.312	1.353	1.351	1.351
C1–C2	1.463	1.471	1.459	1.469	1.473	1.473
Total energy (eV)	-5.136 $\times 10^4$	-5.136 $\times 10^4$	-5.350 $\times 10^4$	-5.350 $\times 10^4$	-6.852 $\times 10^4$	-6.852 $\times 10^4$
HOMO (eV)	-7.3607	-7.4374	-7.4314	-7.4423	-7.0407	-7.0627
LUMO (eV)	-4.3607	-4.3495	-4.4262	-4.4382	-4.0387	-3.8885
Band gap (eV)	2.9941	3.0879	3.0052	3.0041	3.0020	3.1742

*HS, High Spin (S = 1); #LS, Low Spin (S = 0).

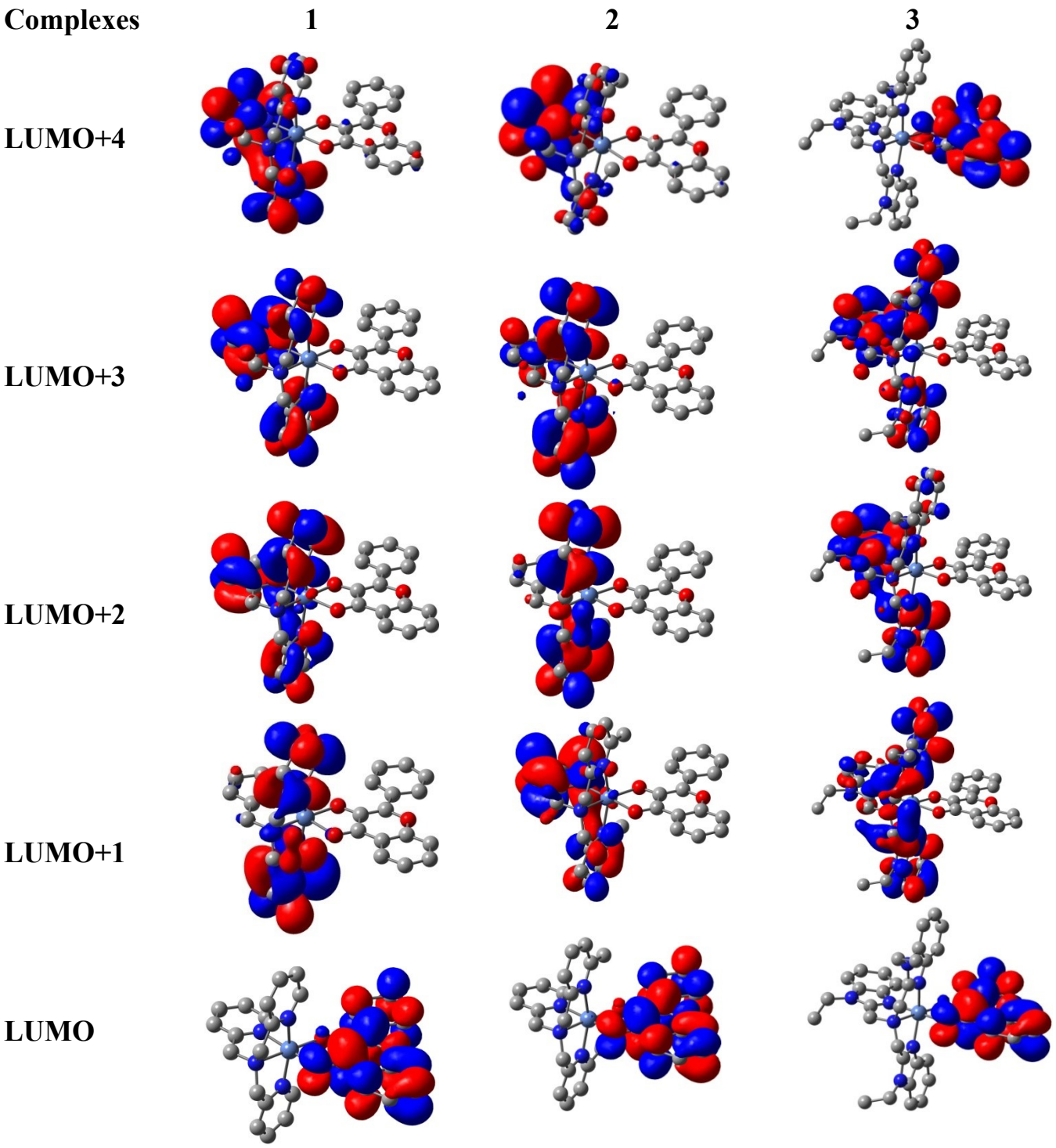

Figure S3. Computed frontier molecular orbitals (LUMO) of complexes $[Ni(L1)(fla)]^+$ **1**, $[Ni(L2)(fla)]^+$ **2** and $[Ni(L3)(fla)]^+$ **3**.

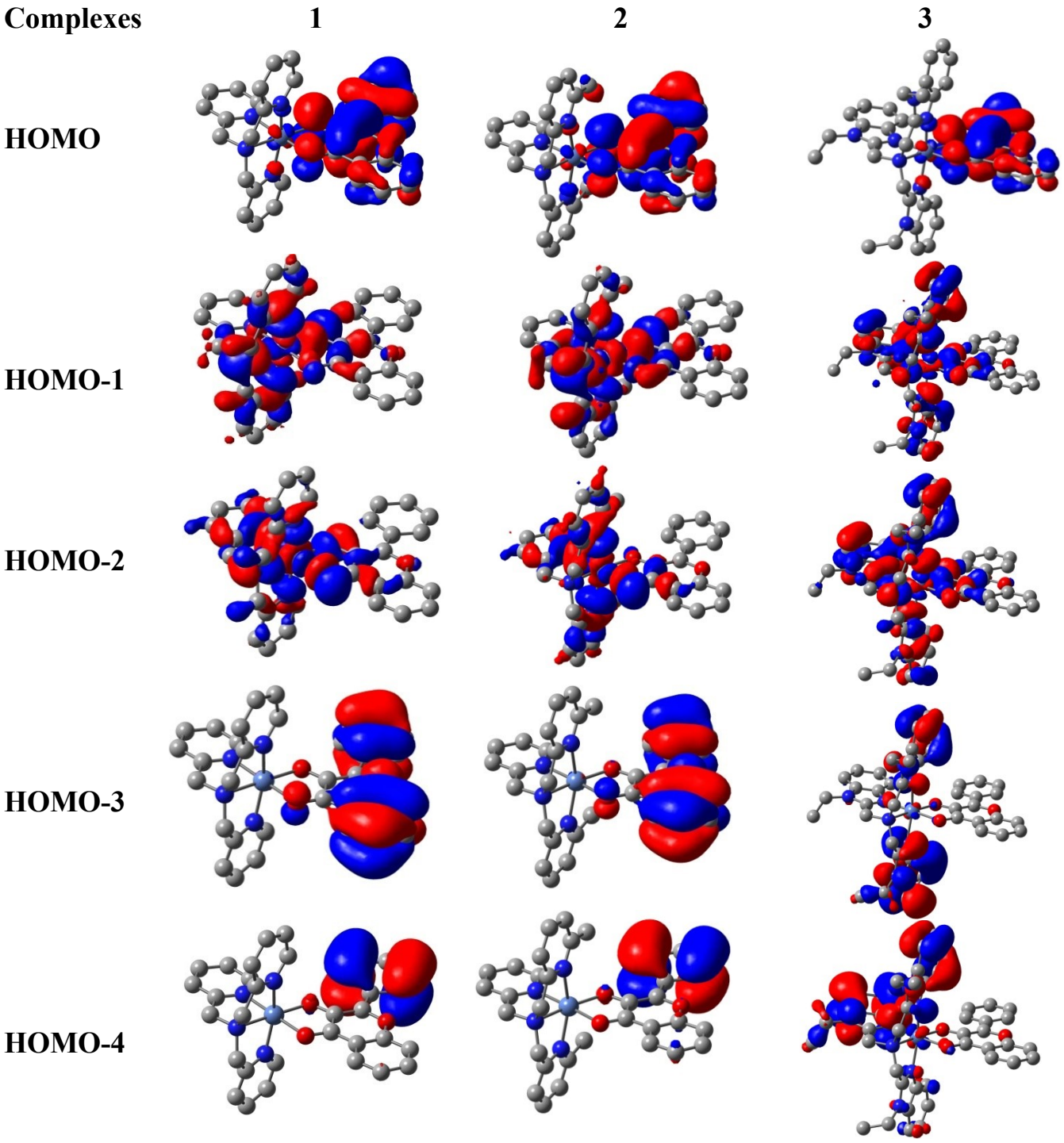

Figure S4. Computed frontier molecular orbitals (HOMO) of complexes $[Ni(L1)(fla)]^+$ **1**, $[Ni(L2)(fla)]^+$ **2** and $[Ni(L3)(fla)]^+$ **3**.

Table S4. Computed HOMO energies for the complexes **1**–**3**.

MOs (eV)	**1**	**2**	**3**
HOMO	-5.582	-5.613	-5.508
HOMO-1	-6.439 (x^2-y^2)	-6.644 (z^2)	-6.572 (x^2-y^2)
HOMO-2	-6.717 (z^2)	-6.832 (x^2-y^2)	-6.606
HOMO-3	-6.997	-7.025	-6.690
HOMO-4	-7.170	-7.190	-6.734
HOMO-5	-7.583	-7.360	-6.804
HOMO-6	-7.604	-7.438	-6.827 (z^2)
HOMO-7	-7.645	-7.623	-6.871
HOMO-8	-7.787	-7.634	-6.930
HOMO-9	-7.837(xy)	-7.711	-6.974
HOMO-10	-7.859	-7.833(yz, xz)	-7.151
HOMO-11	-8.289(yz, xz)	-8.220	-7.585
HOMO-12	-8.334	-8.345(xy)	-7.685
HOMO-13	-8.366(yz, xz)	-8.362	-7.793(xy)
HOMO-14	-8.633	-8.546	-8.407(yz, xz)
HOMO-15	-8.714	-8.655	-8.474(yz, xz)
HOMO-16	-8.985	-9.010	-8.558

Table S5. Torsion angles [°] **1–3**.

C1-C3-C4-C5	Experimental	Calculated
1	1.050(9)	0.279
2	-	-0.005
3	-5.480(13)	-5.230

Table S6. Computed bond angles [°] of complexes **1–3**

Bond angles/°	1	2	3
N1–Ni–N2	81.3240	80.0806	79.8494
N1–Ni–N3	91.0590	88.6330	89.9420
N1–Ni–N4	162.2969	160.2493	157.9899
N1–Ni–O1	98.6281	99.8225	100.6478
N1–Ni–O2	89.1680	90.8504	88.2390
N2–Ni–N3	83.3965	84.4062	81.6066
N2–Ni–N4	81.3875	80.2392	79.0045
N2–Ni–O1	178.2134	172.3422	175.8644
N2–Ni–O2	97.4691	92.1219	95.3606
N3–Ni–N4	90.7145	87.8136	92.7174
N3–Ni–O1	98.3900	103.2513	102.4805
N3–Ni–O2	179.1293	176.5272	176.7017
N4–Ni–O1	98.5328	99.9039	100.0091
N4–Ni–O2	89.3237	91.5255	87.7174
O1–Ni–O2	80.7444	80.2207	80.5677

Table S7. Computed bond angles [°] of geometric isomers **1b–3b**.

Bond angles/°	1b		2b		3b	
	*HS	#LS	*HS	#LS	*HS	#LS
N1–Ni–N2	81.576	82.210	80.470	81.752	79.581	78.832
N1–Ni–N3	89.716	90.395	87.302	90.278	89.687	89.912
N1–Ni–N4	163.105	163.994	160.633	164.940	159.106	157.061
N1–Ni–O1	98.419	97.826	99.670	93.246	100.069	100.002
N1–Ni–O2	90.013	89.876	91.855	90.514	89.106	89.186
N2–Ni–N3	83.242	79.233	83.956	81.458	81.623	76.454
N2–Ni–N4	81.585	82.192	80.475	83.225	79.654	78.861
N2–Ni–O1	177.543	179.663	172.480	161.577	174.007	176.370
N2–Ni–O2	94.963	100.907	90.853	90.047	91.673	98.366
N3–Ni–N4	89.657	90.204	87.287	88.532	89.572	90.030
N3–Ni–O1	99.214	100.431	103.564	116.436	104.368	107.037
N3–Ni–O2	178.206	179.710	174.808	171.265	173.297	174.818
N4–Ni–O1	98.346	97.793	99.675	100.722	100.338	101.934
N4–Ni–O2	90.087	89.564	91.858	88.443	89.206	88.814
O1–Ni–O2	82.580	79.43	81.628	72.199	82.336	78.144

*HS, High Spin (S = 1); #LS, Low Spin (S = 0).

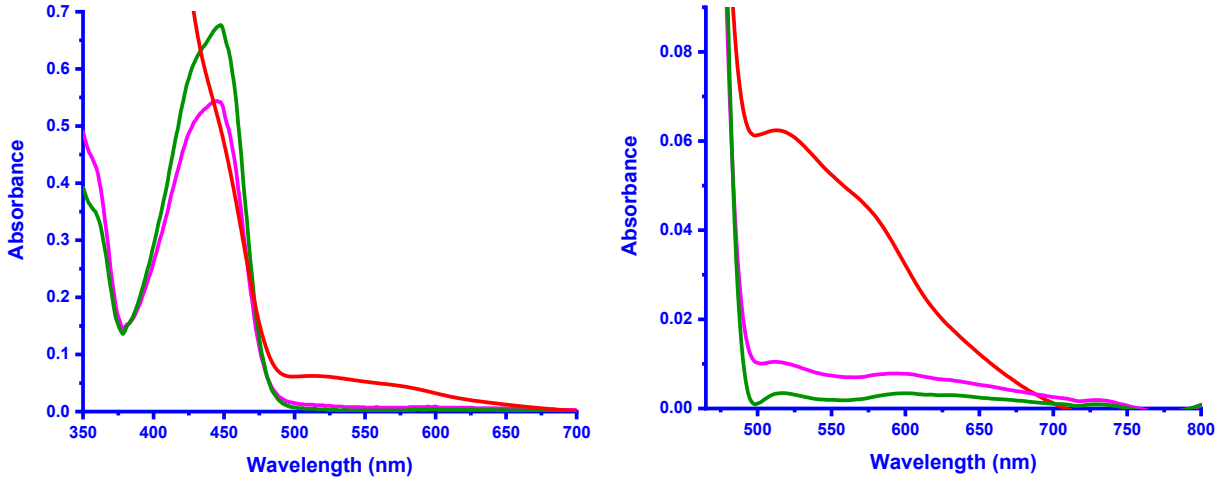

Figure S5. Spectral changes of **3** (1.4×10^{-4} M) in the presence of NBT^{2+} (3.0×10^{-4} M) (red) in DMF at 70 °C under O_2 (pink) and N_2 (green).

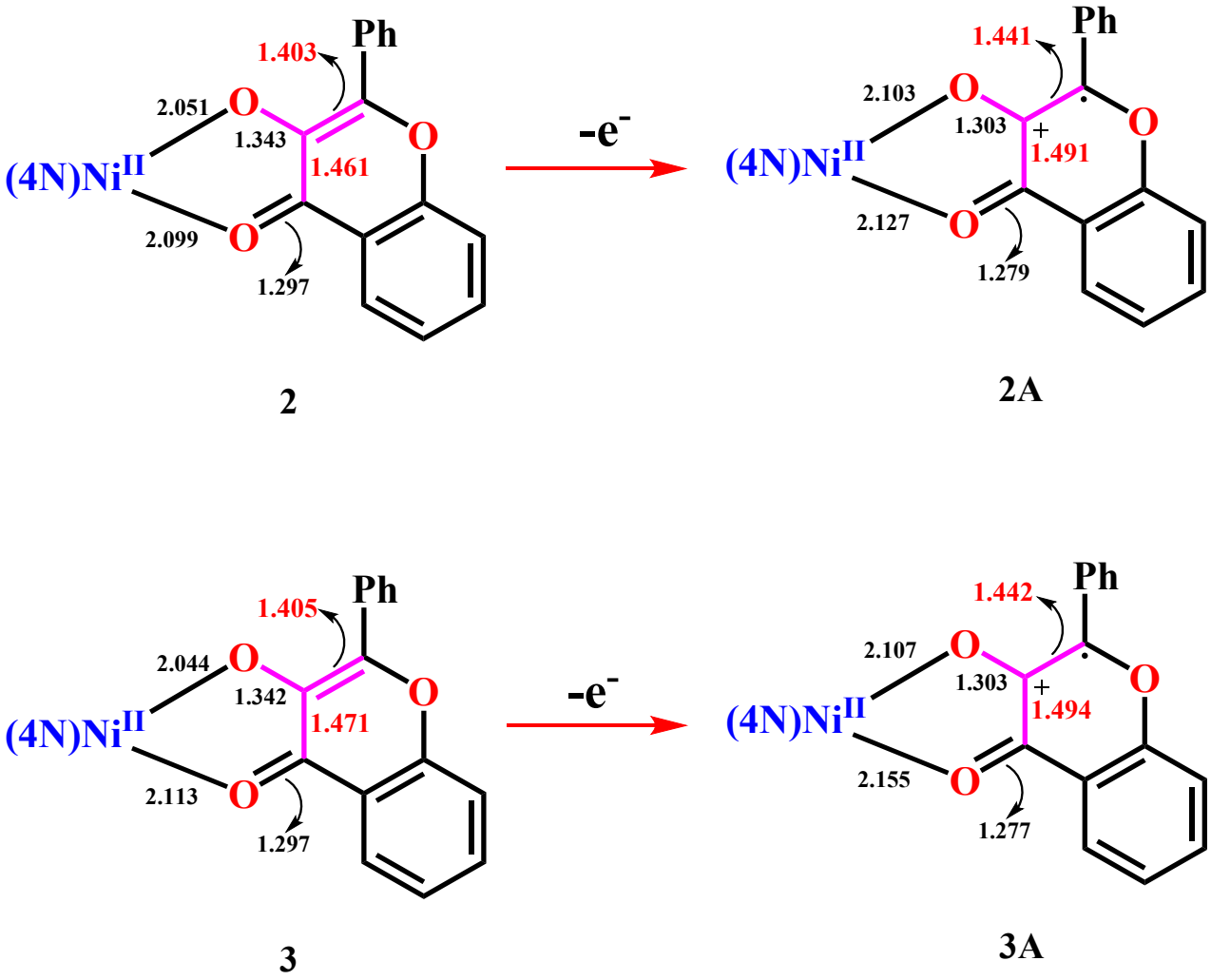

Scheme S1. Changes in bond length upon removal of an electron from Ni(II)-bound flavonolate in **2–3** to form the radical **2A–3A**.

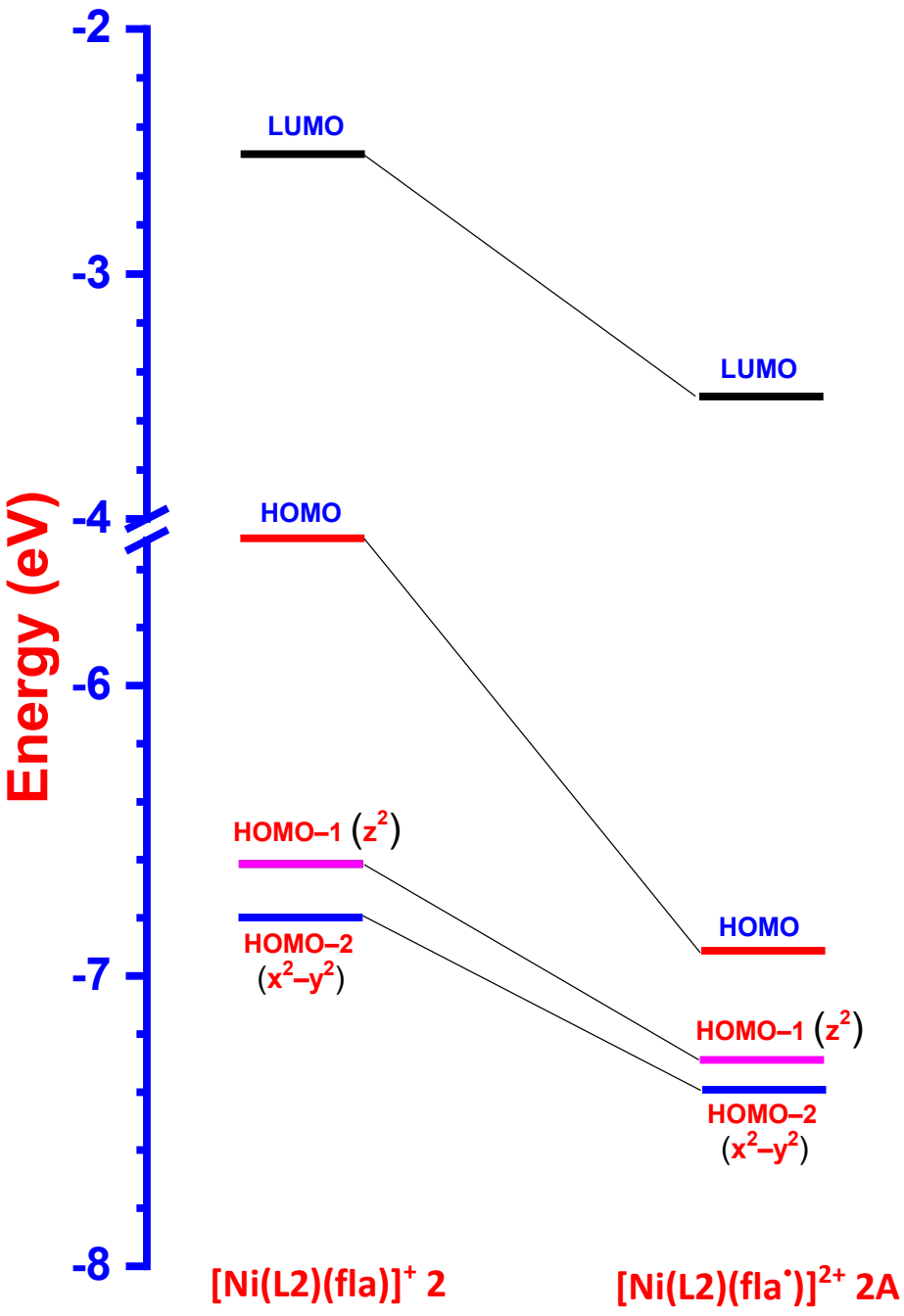

Figure S6. HOMO and LUMO energy profile diagram for the complexes **2** and **2A**

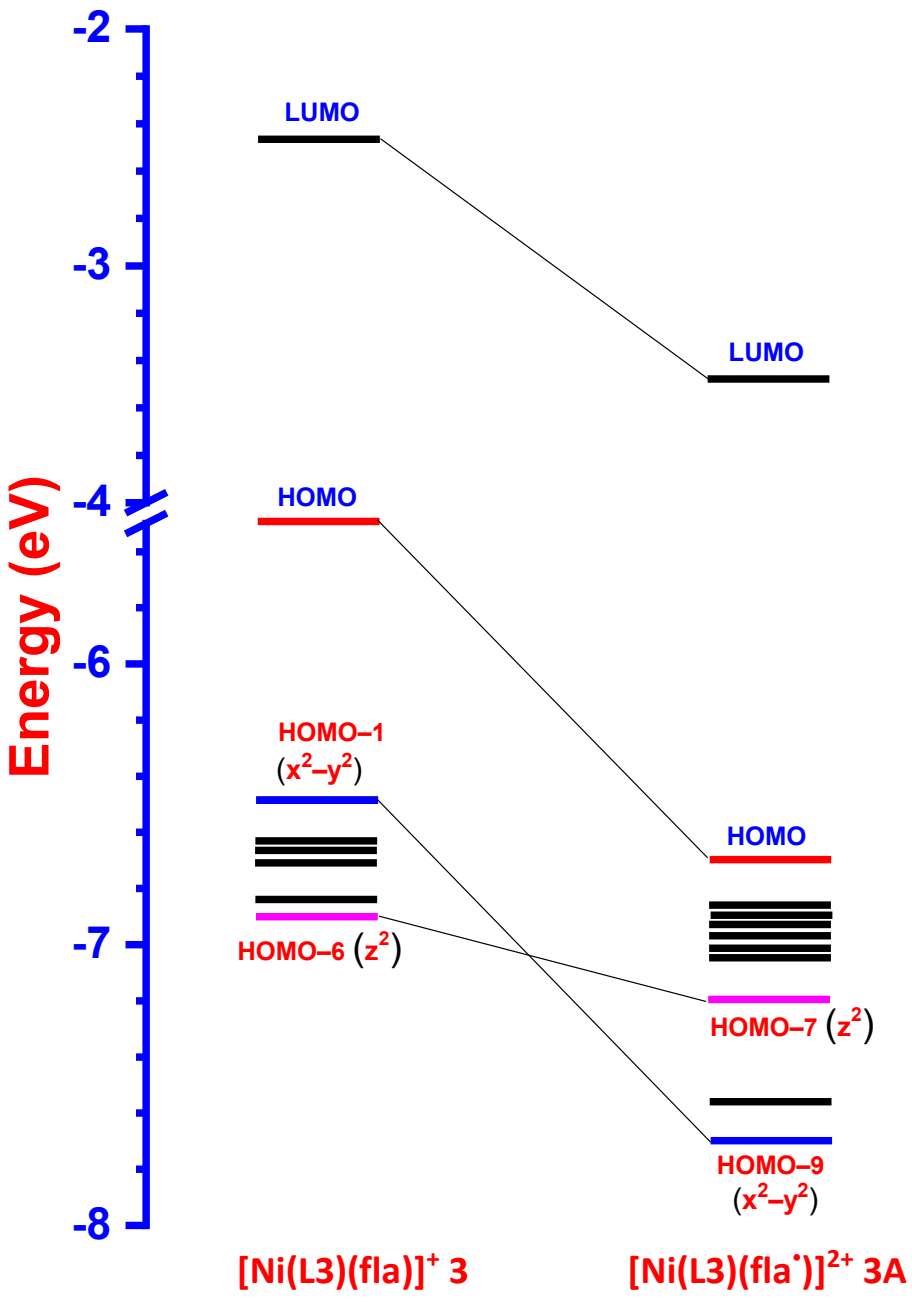

Figure S7. HOMO and LUMO energy profile diagram for the complexes **3** and **3A**

Table S8. Important bond lengths (Å) of coordinated flavonolate for the complexes $[Ni(L)(fla)]^{+}$ **1**–**3** and the radical intermediates $[Ni(L)(fla^{\bullet})]^{2+}$ **1A**–**3A.**

Computed species	**Bond lengths/Å**					
	Ni–O1	Ni–O2	C2=O2	C1–O1	C1–C2	C1–C3
1	2.044	2.113	1.297	1.342	1.471	1.404
1A	2.099	2.146	1.279	1.303	1.494	1.442
2	2.051	2.099	1.297	1.343	1.467	1.403
2A	2.103	2.127	1.279	1.303	1.491	1.441
3	2.049	2.119	1.295	1.341	1.473	1.405
3A	2.107	2.155	1.277	1.303	1.494	1.442

Table S9. Spin density values for selected atoms of coordinated flavonolate for the complexes $[Ni(L)(fla)]^{+}$ **1**–**3** and the radical intermediates $[Ni(L)(fla^{\bullet})]^{2+}$ **1A**–**3A.**

Spin Densities	Ni	O1	O2	C1	C2	C3
1	1.628	0.063	0.054	0.002	-0.003	-0.005
1A	1.616	0.375	0.147	0.108	0.007	0.216
2	1.645	0.054	0.053	0.003	-0.003	-0.005
2A	1.626	0.382	0.143	0.099	0.009	0.216
3	1.660	0.066	0.054	0.003	-0.003	-0.006
3A	1.650	0.384	0.146	0.096	0.003	0.228

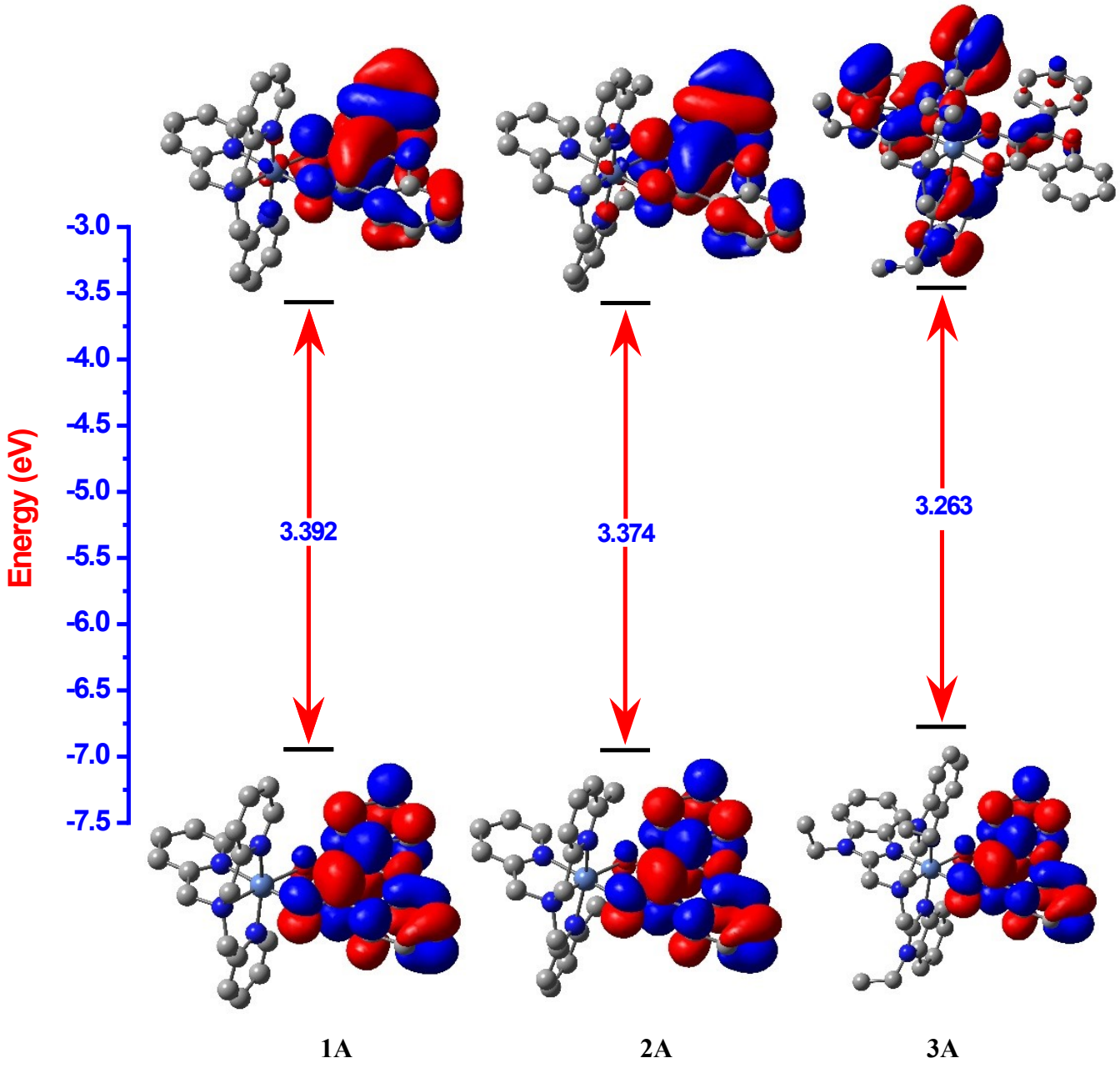

Figure S8. HOMO and LUMO band gap energy profile diagram for $[Ni(L1)(fla^{\bullet})]^{2+}$ **1A**, $[Ni(L2)(fla^{\bullet})]^{2+}$ **2A** and $[Ni(L3)(fla^{\bullet})]^{2+}$ **3A**, calculated at U-B3LYP combined correlation function and basis sets for metal atom LANL2DZ and 6-31G* basis sets for other non-metal atoms and acetonitrile as a solvent by the CPCM method.

Table S10. Computed structural parameters and HOMO and LUMO energies and band gap energies for complexes **1A**–**3A**

Bond lengths/Å	**1A**	**2A**	**3A**
Ni–N1	2.080	2.177	2.061
Ni–N2	2.111	2.088	2.205
Ni–N3	2.045	2.051	2.043
Ni–N4	2.082	2.177	2.061
Ni–O1	2.099	2.103	2.107
Ni–O2	2.146	2.127	2.155
O1–C1	1.303	1.303	1.303
O2–C2	1.279	1.279	1.277
C1–C2	1.494	1.491	1.494
C1–C3	1.442	1.441	1.442
Total energy (eV)	-5.136×10^4	-5.350×10^4	-6.851×10^4
HOMO (eV)	-6.938	-6.934	-6.754
LUMO (eV)	-3.545	-3.559	-3.491
Band gap (eV)	3.392	3.374	3.263

Table S11. Computed bond angles [°] of complexes **1A–3A**

Bond angles/°	**1A**	**2A**	**3A**
N1–Ni–N2	82.3268	81.6981	80.998
N1–Ni–N3	91.5634	89.9963	92.192
N1–Ni– N4	164.0711	163.2898	160.477
N1–Ni–O1	97.1919	98.1126	98.4029
N1–Ni–O2	88.8852	89.6913	87.2496
N2–Ni–N3	84.8385	85.2370	83.4283
N2–Ni–N4	82.3673	81.6578	80.8129
N2–Ni–O1	174.3929	170.4035	171.4985
N2–Ni–O2	96.5932	92.7246	93.8604
N3–Ni–N4	91.4302	90.0953	92.7198
N3–Ni–O1	100.7641	104.3594	105.0731
N3–Ni–O2	178.5457	177.9615	177.2860
N4–Ni–O1	97.6088	98.0488	98.5323
N4–Ni–O2	88.5118	89.6249	86.9523
O1–Ni–O2	77.8052	77.6791	77.6380
Torsion angles [°] (C1-C3-C4-C5)	1.678	-0.004	-1.182

Figure S9. The time course of absorbance of UV-Vis band observed at 450 nm in the presence of O_2 in DMF solution of [Ni(L3)(fla)]ClO_4 **3** (1×10^{-4} M) at 70 ºC.

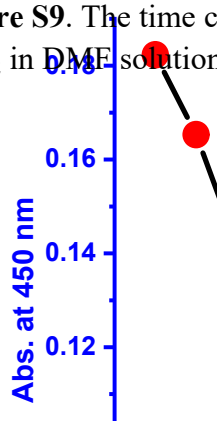

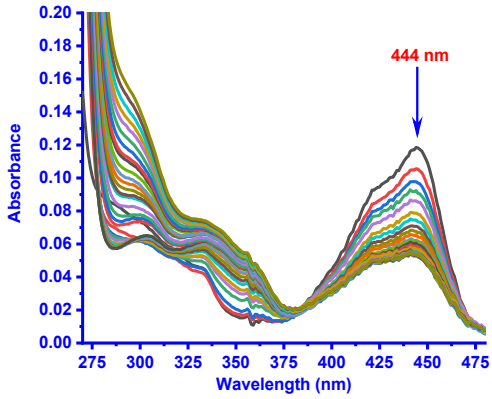
444 nm
Absorbance
Wavelength (nm)
0.00
0.02
0.04
0.06
0.08
0.10
0.12
0.14
0.16
0.18
0.20
275
300
325
350
375
400
425
450
475

(a)

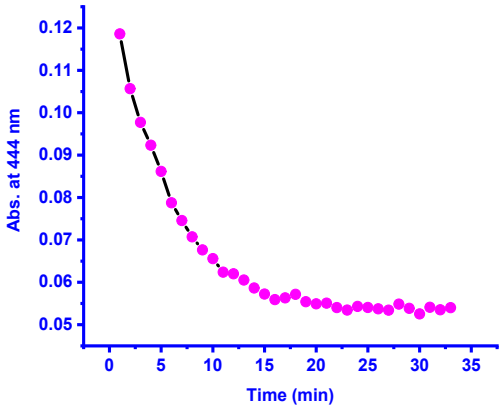
Abs. at 444 nm
Time (min)
0.05
0.06
0.07
0.08
0.09
0.10
0.11
0.12
0
5
10
15
20
25
30
35

(b)

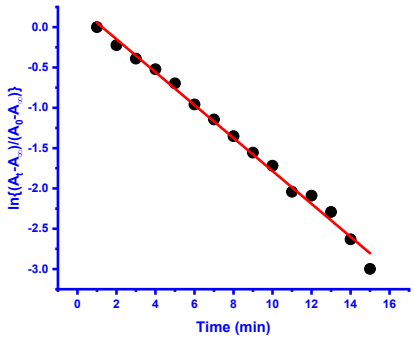
ln{(A_t-A_∞)/(A_0-A_∞)}
Time (min)
0.0
-0.5
-1.0
-1.5
-2.0
-2.5
-3.0
0
2
4
6
8
10
12
14
16

(c)

Figure S10. **a)** UV-Vis spectral changes observed in the presence of O_2 in DMF solution of [Ni(L1)(fla)]ClO_4 **1** (1×10^{-4} M) at 70 ºC; **b)** The time course of absorbance at 444 nm and **c)** Plot of $\ln\{(A_t-A_\infty)/(A_0-A_\infty)$ vs time vs time for the band observed at 444 nm**.**

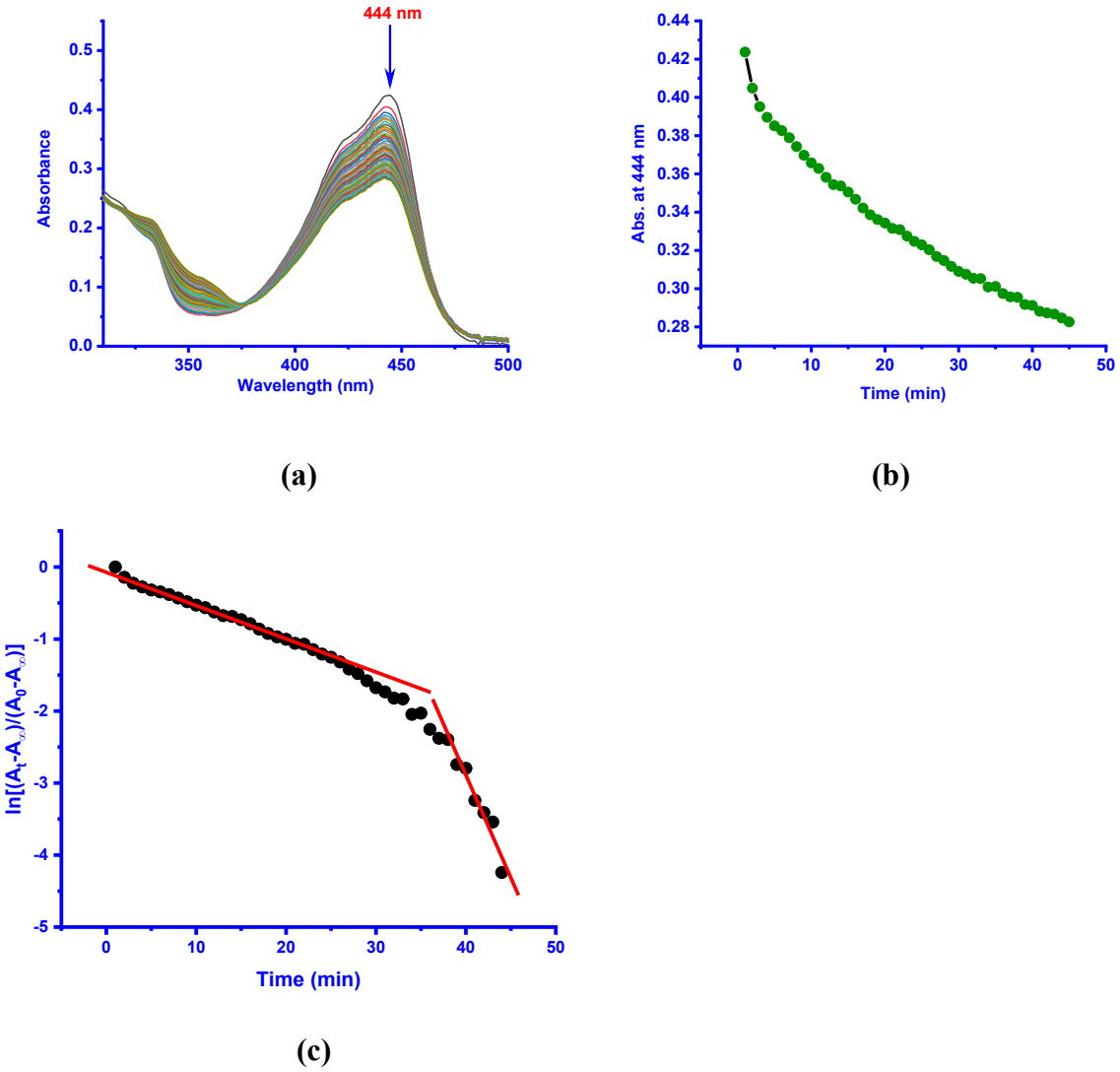

(a) **(b)**

(c)

Figure S11. **a)** UV-Vis spectral changes observed in the presence of atmospheric O_2 in DMF solution of [Ni(L2)(fla)]ClO_4 **2** (1×10^{-4} M) at 70 ºC; **b)** The time course of absorbance at 444 nm and **c)** Plot of $\ln\{(A_t-A_\infty)/(A_0-A_\infty)\}$ vs time for the band observed at 444 nm**.**

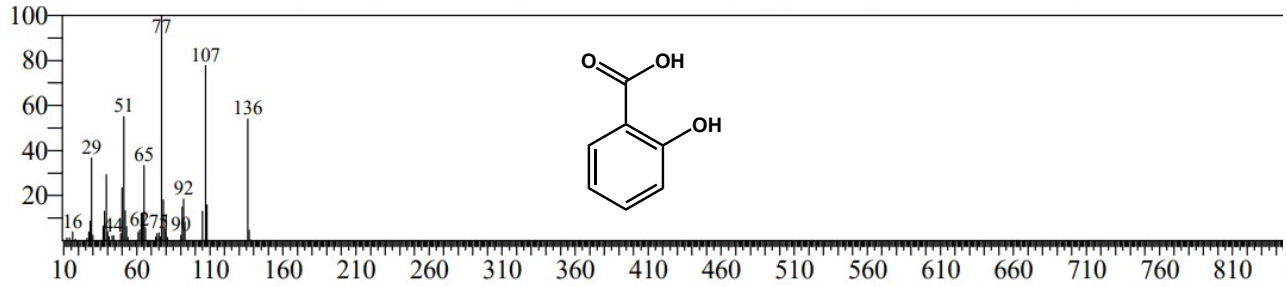

(**a**)

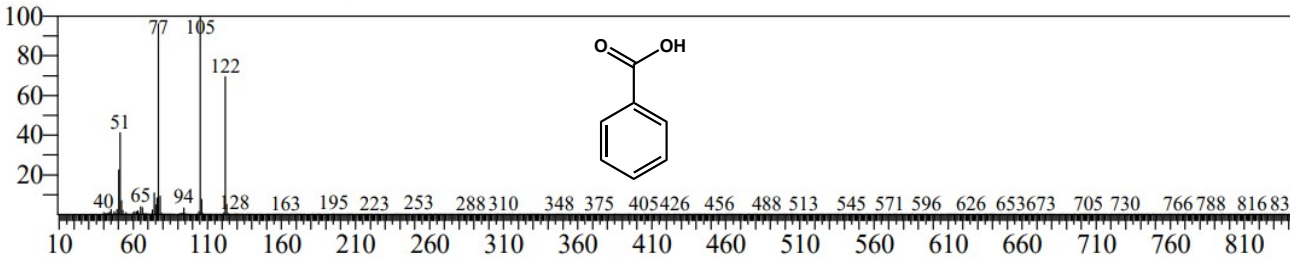

(**b**)

Figure S12. GC-MS product analysis of the products of reactions between dioxygen ES model complexes $[Ni(L)(fla)]^+$ **1–3** in DMF at 70 ºC to give rise to (**a**) salicylic acid [*m/z* (neg.): 136 $(M - 2H)^-$] (20–60%), (**b**) benzoic acid [*m/z* (neg.): 122 (M^+)] (21–43%), as ultimate products (**Scheme 2**).

Table S12. GC-MS analysis of the products of reaction between dioxygen and ES model complexes $[Ni(L)(fla)]^+$ **1–3** (1.0×10^{-3} M) in DMF solution at 70 ºC.

Complex	**Yield (%)**

	Salicylic acid	Benzoic acid	2-Hydroxy-*N*,*N*-dimethyl-benzamide	*N*,*N*-Dimethyl-benzamide
[Ni(L1)(fla)](ClO_4) **1**	45	30	12	-
[Ni(L2)(fla)](ClO_4) **2**	20	43	4	8
[Ni(L3)(fla)](ClO_4) **3**	60	21	-	14

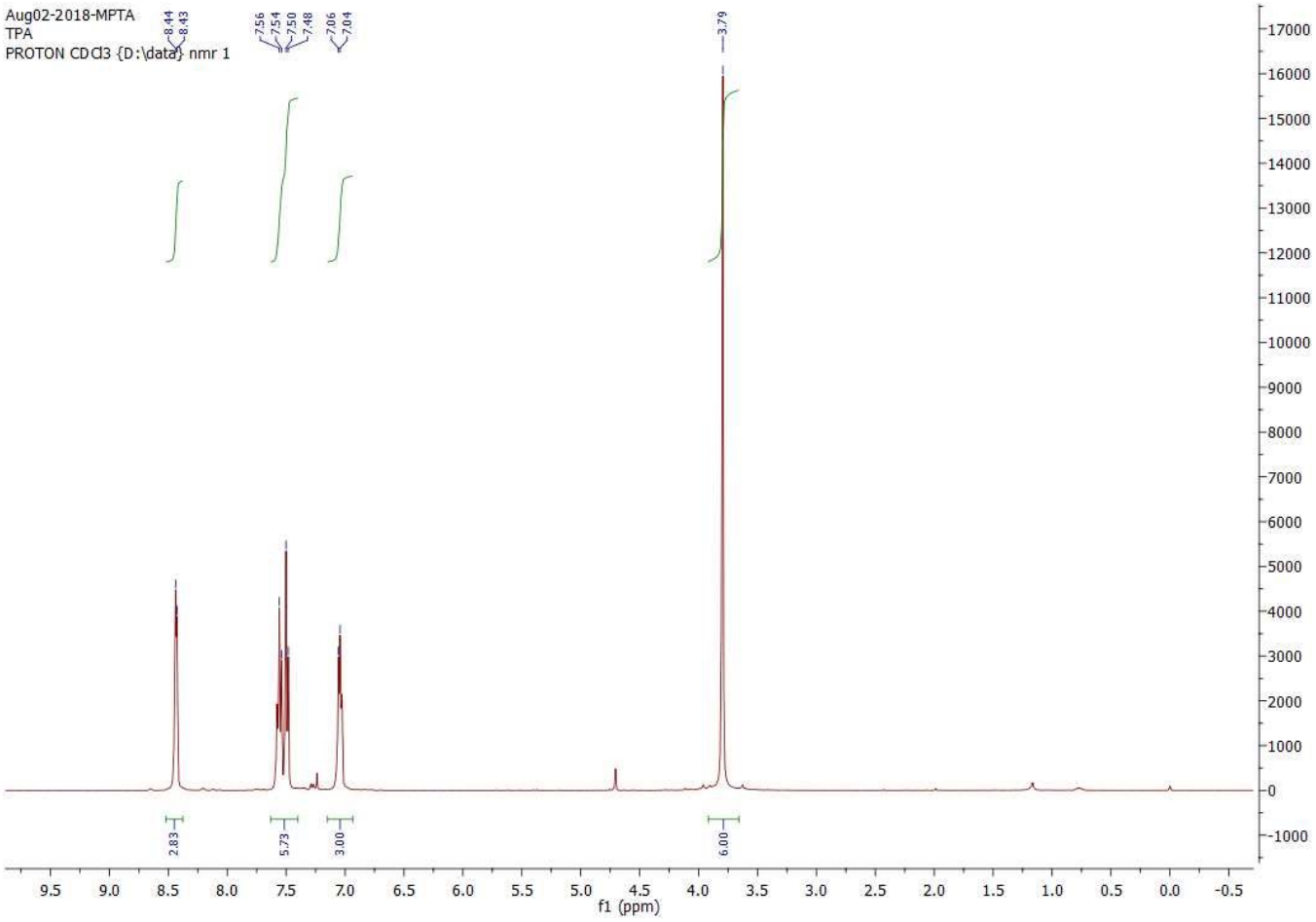

Figure S13. ^{1}H NMR spectra for the ligand **L1**.

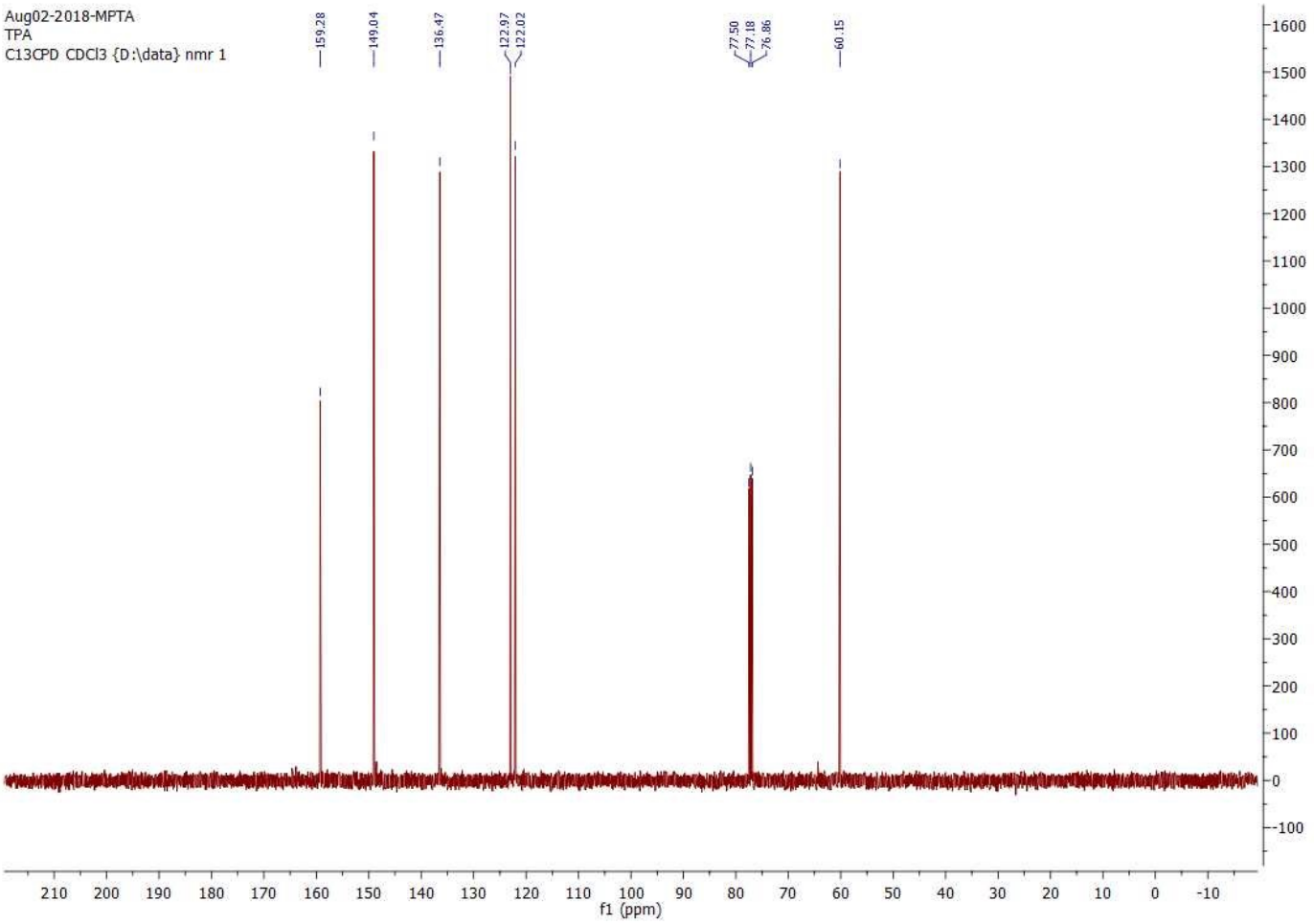

Figure S14. ^{13}C NMR spectra for the ligand **L1**.

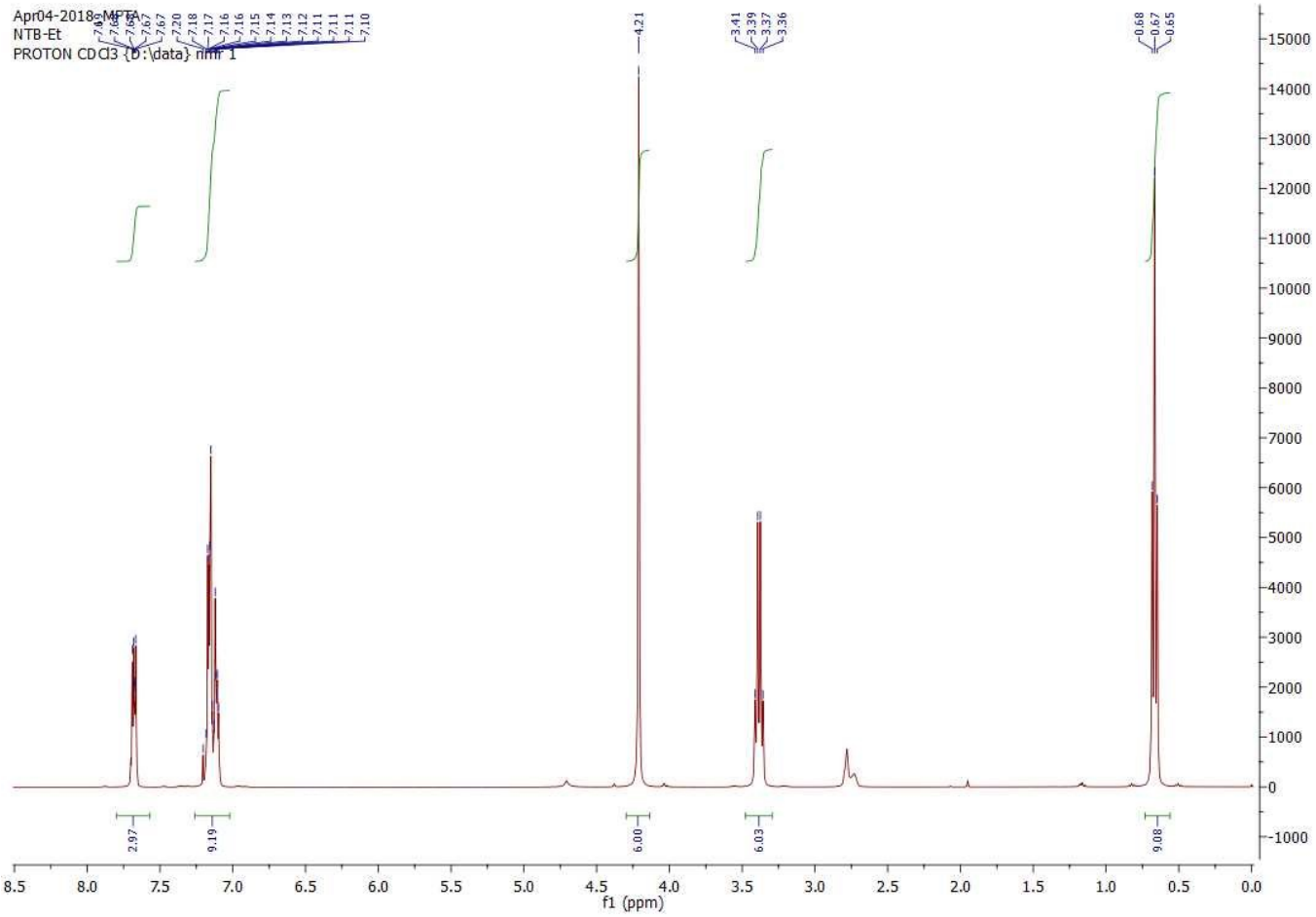

Figure S15. ^{1}H NMR spectra for the ligand **L3**.

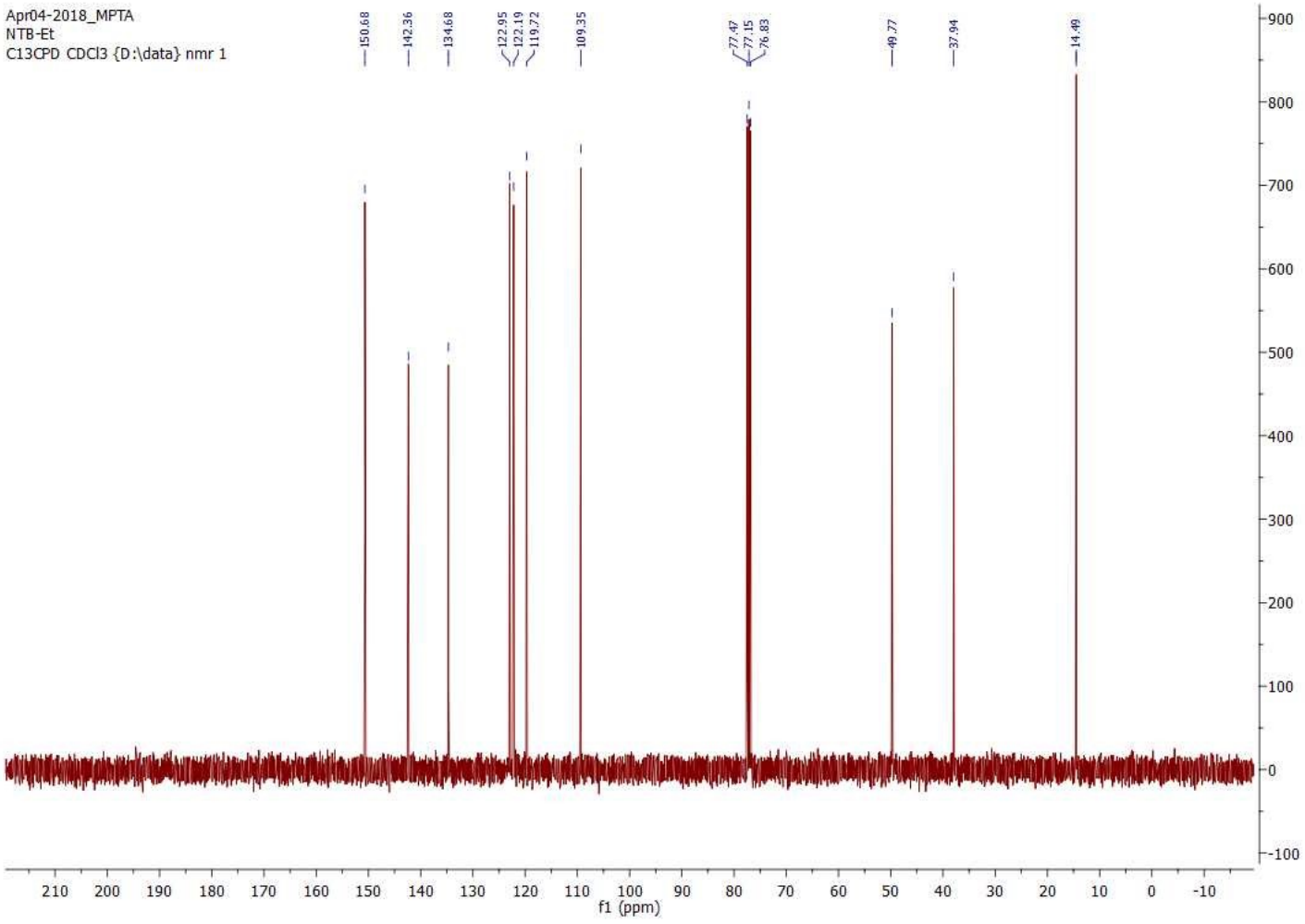

Figure S16. ^{13}C NMR spectra for the ligand **L3**.

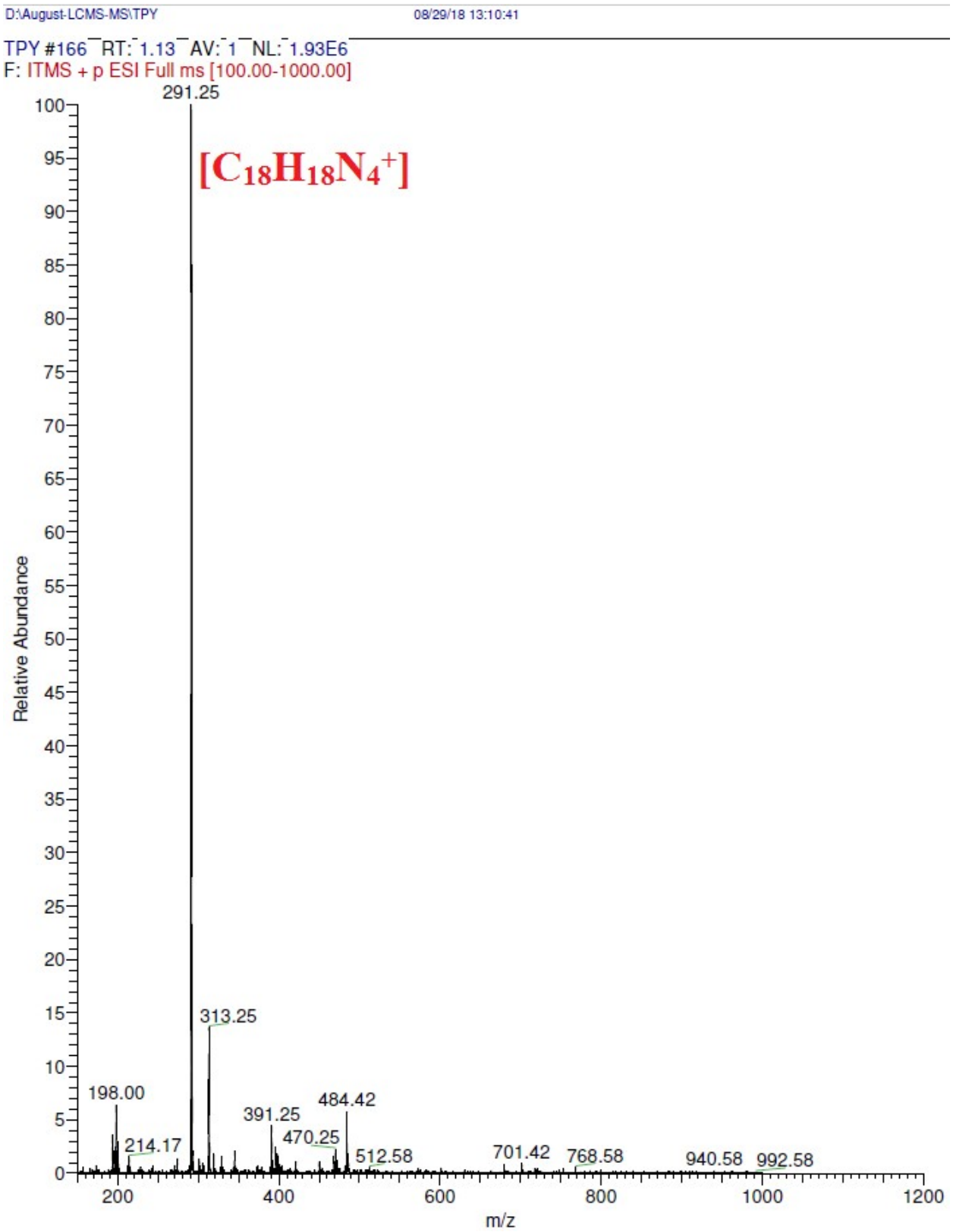

Figure S17. LC-MS of tris(2-pyridylmethyl)amine(tpa) **L1** in methanol solution (1×10^{-3} M) at 25 ºC.

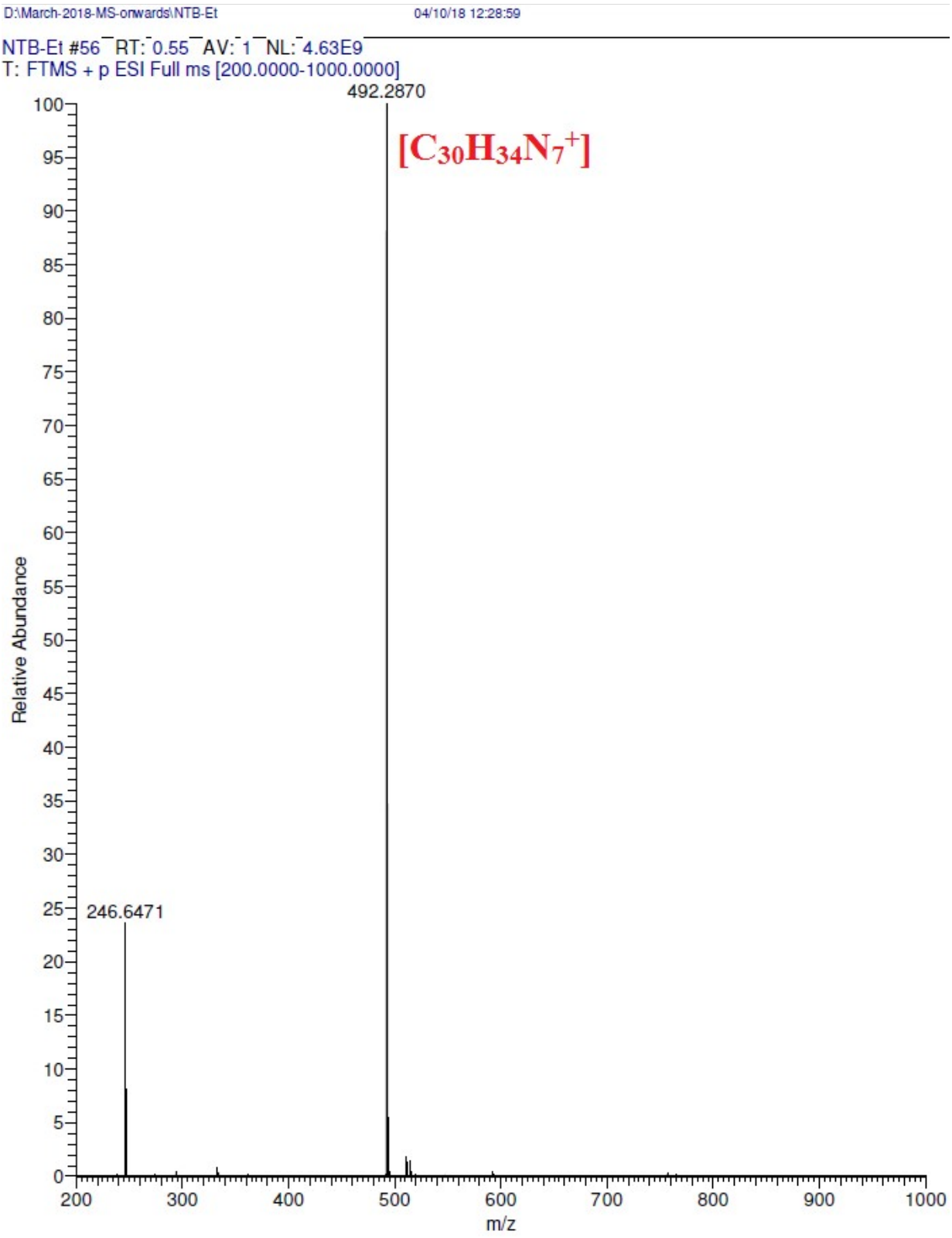

Figure S18. High Resolution Mass Spectra of tris(*N*-Et-benzimidazol-2-ylmethyl)amine (Et-ntb) **L3** in methanol solution (1×10^{-3} M) at 25 ºC.

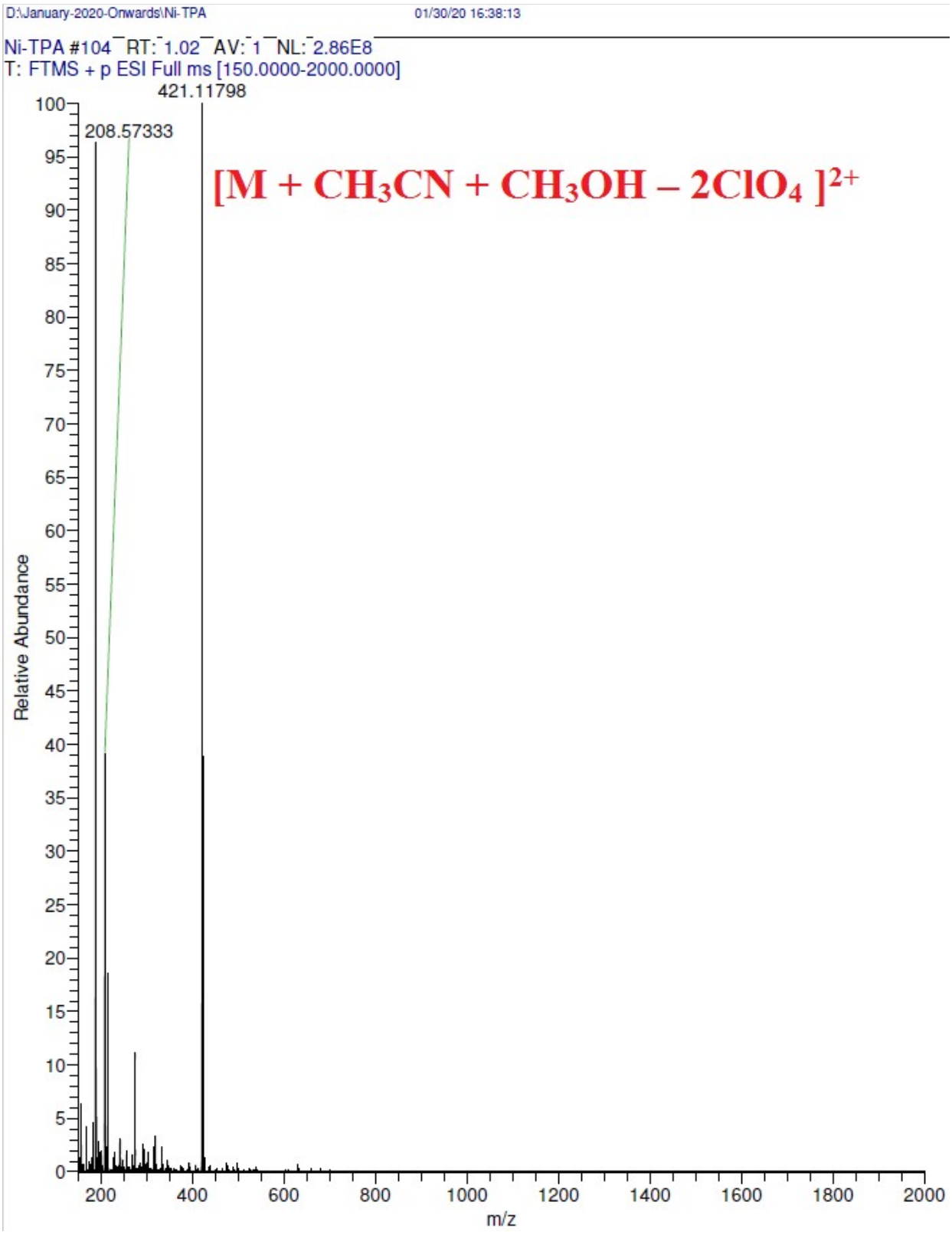

Figure S19. High Resolution Mass Spectra of $[Ni(L1)](ClO_4)_2$ **1a** in acetonitrile solution (1×10^{-3} M) at 25 ºC.

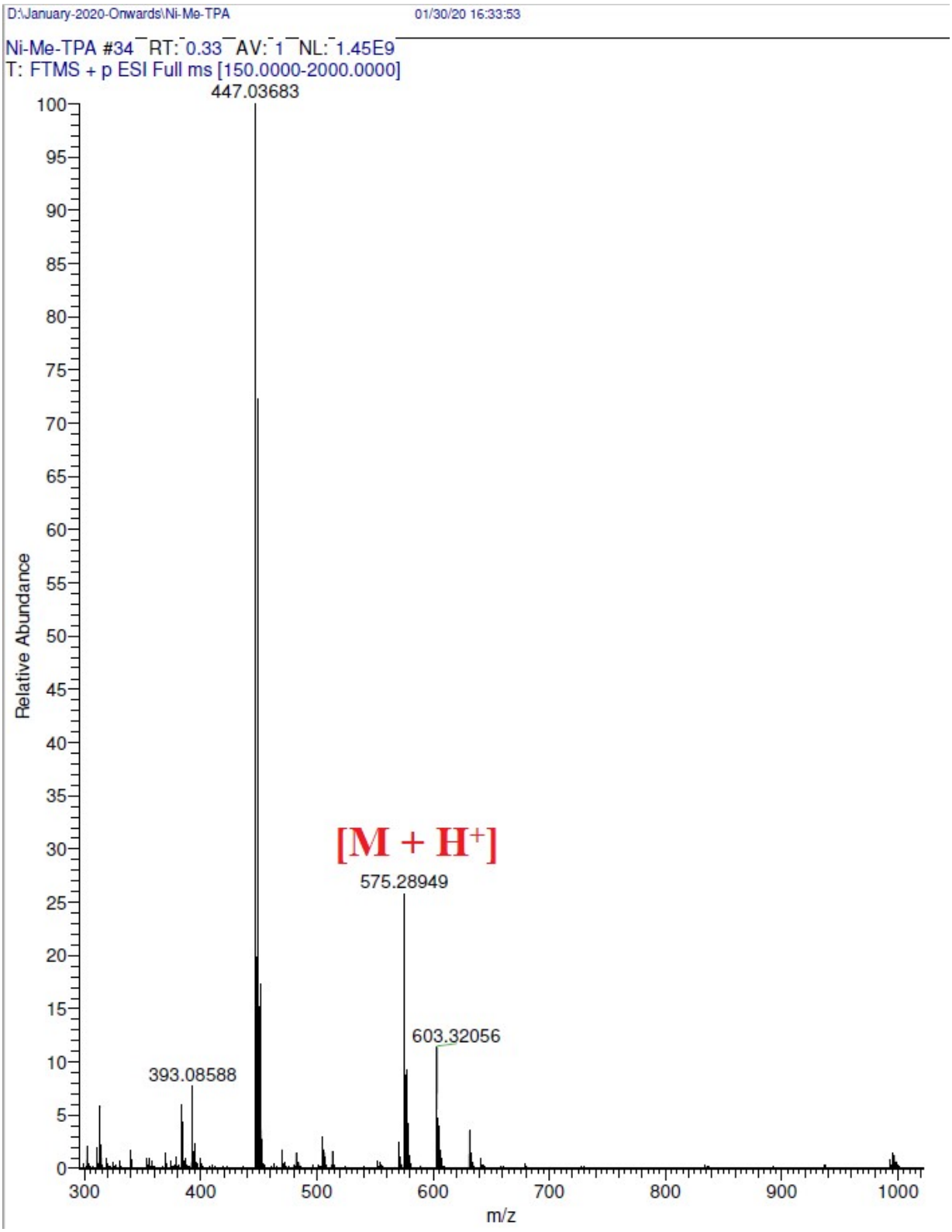

Figure S20. High Resolution Mass Spectra of $[Ni(L2)](ClO_4)_2$ **2a** in acetonitrile solution (1×10^{-3} M) at 25 ºC.

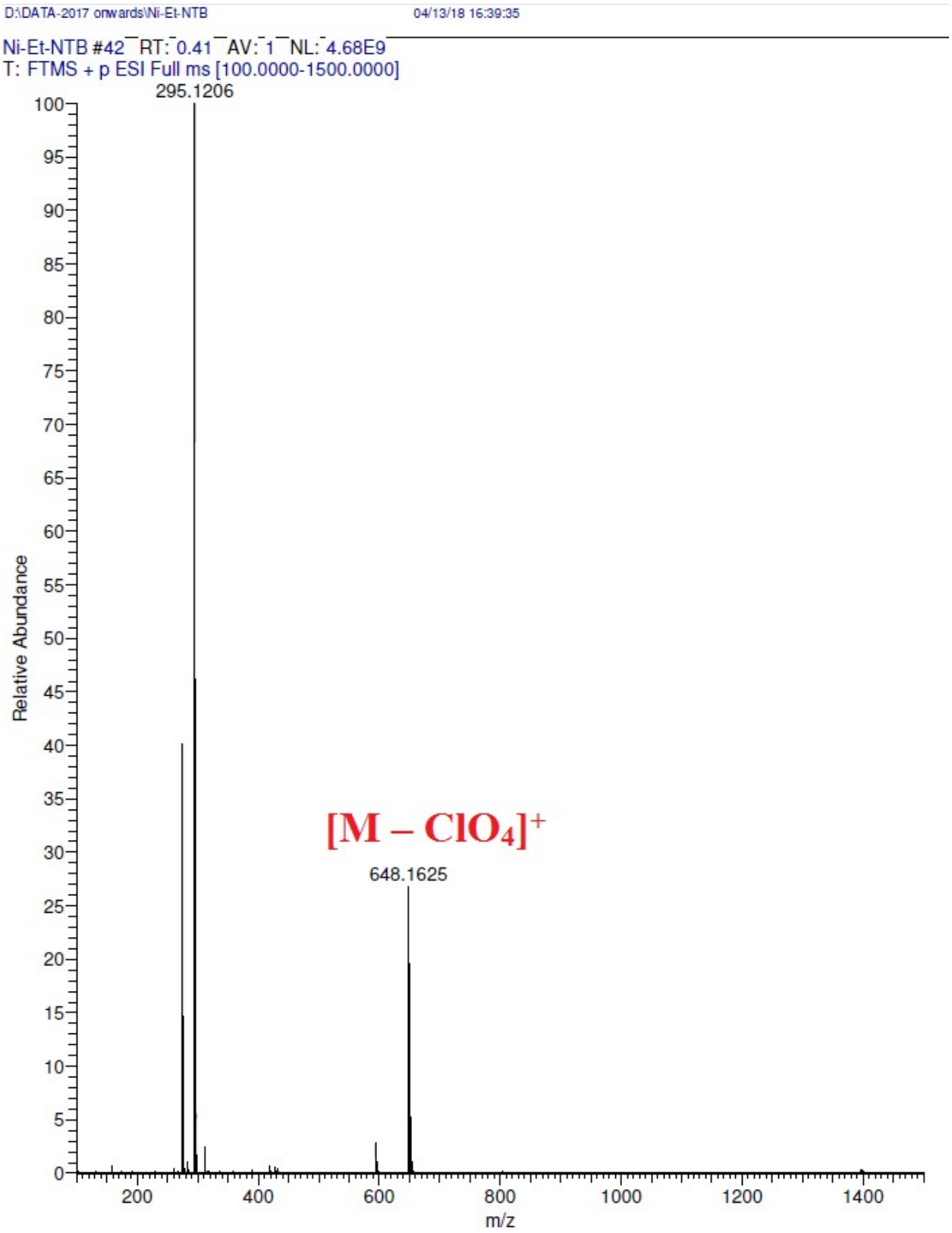

Figure S21. High Resolution Mass Spectra of $[Ni(L3)](ClO_4)_2$ **3a** in acetonitrile solution (1×10^{-3} M) at 25 ºC.

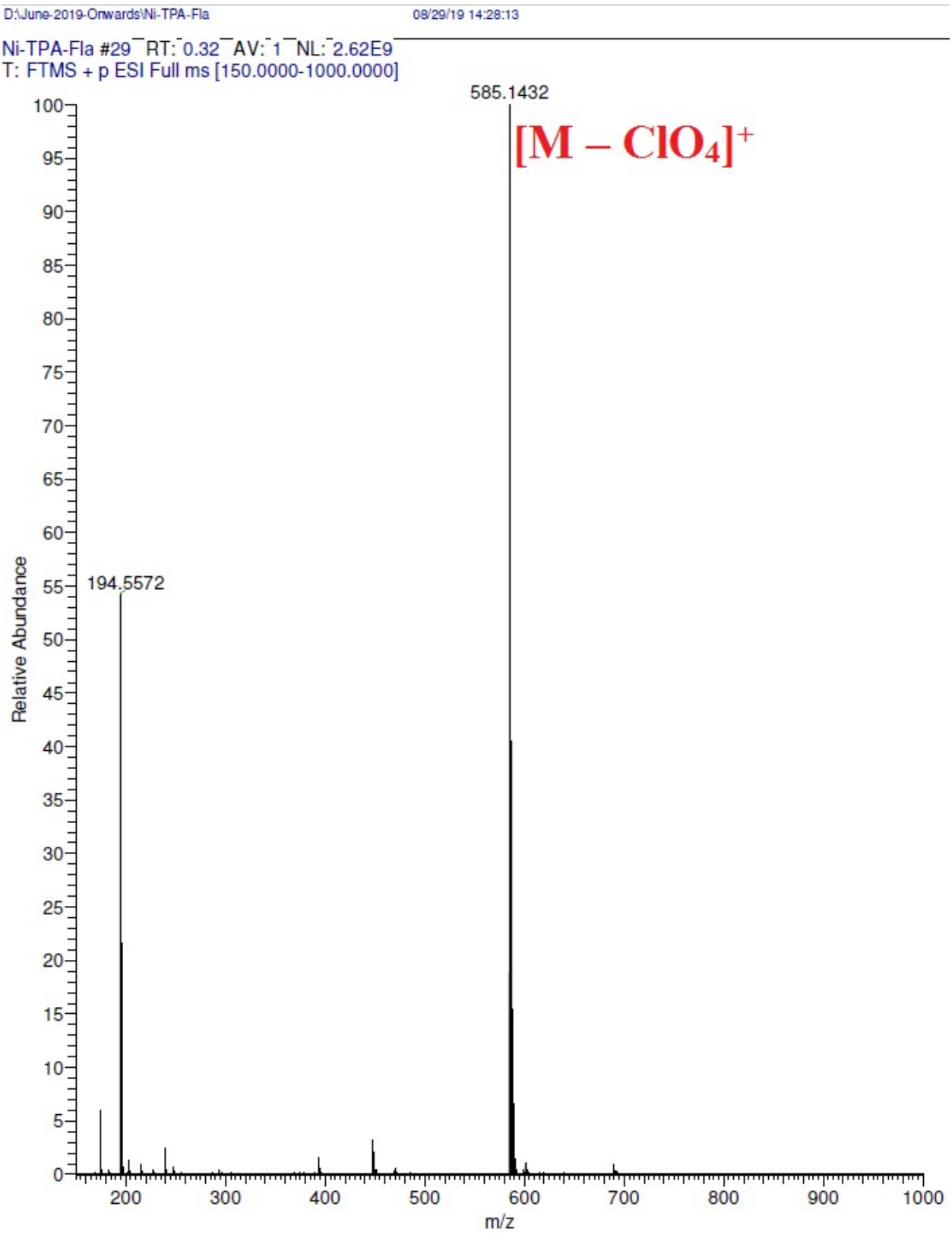

Figure S22. High Resolution Mass Spectra of [Ni(L1)(fla)]ClO_4 **1** in acetonitrile solution (1×10^{-3} M) at 25 ºC.

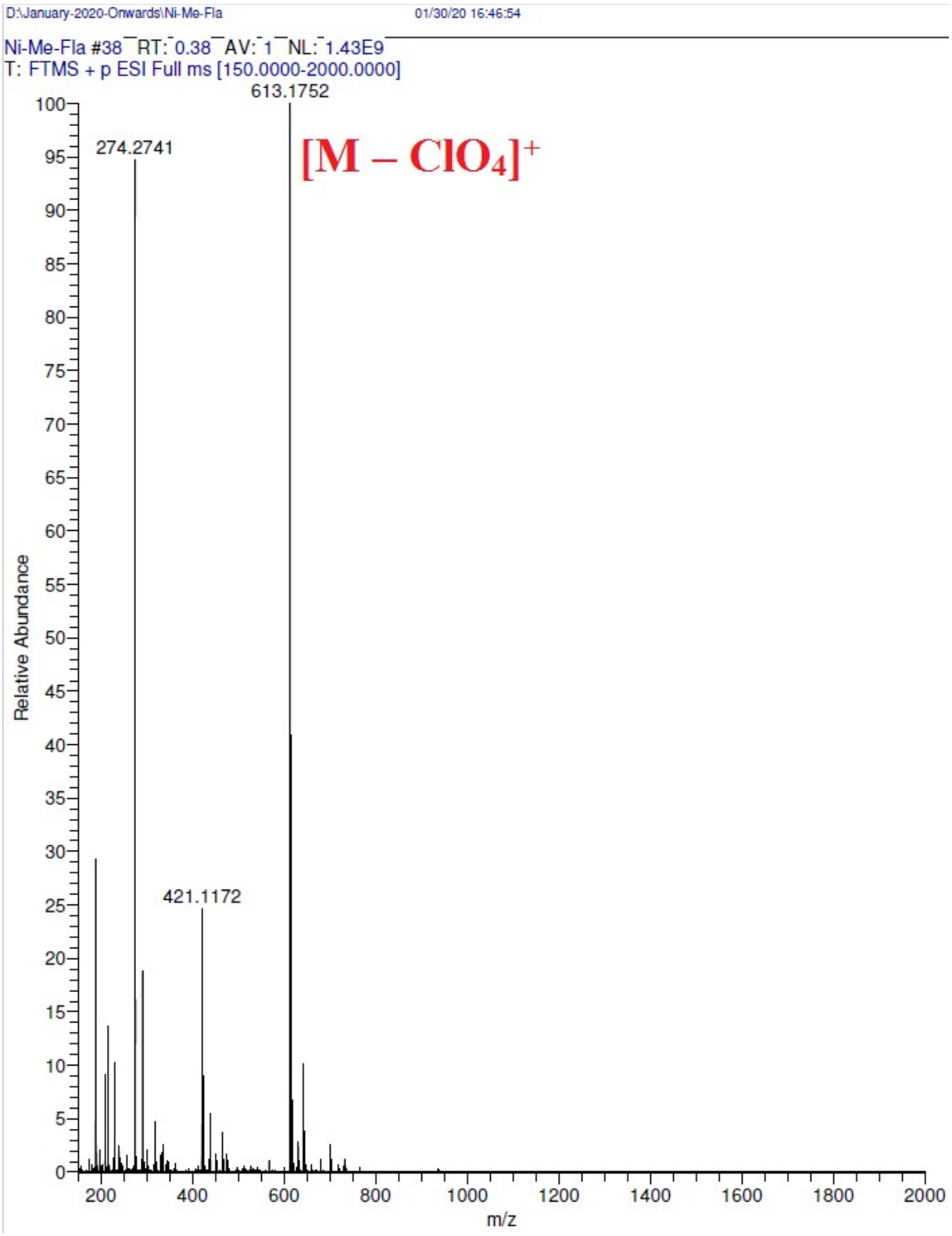

Figure S23. High Resolution Mass Spectra of [Ni(L2)(fla)]ClO_4 **2** in acetonitrile solution (1 × 10^{-3} M) at 25 ºC.

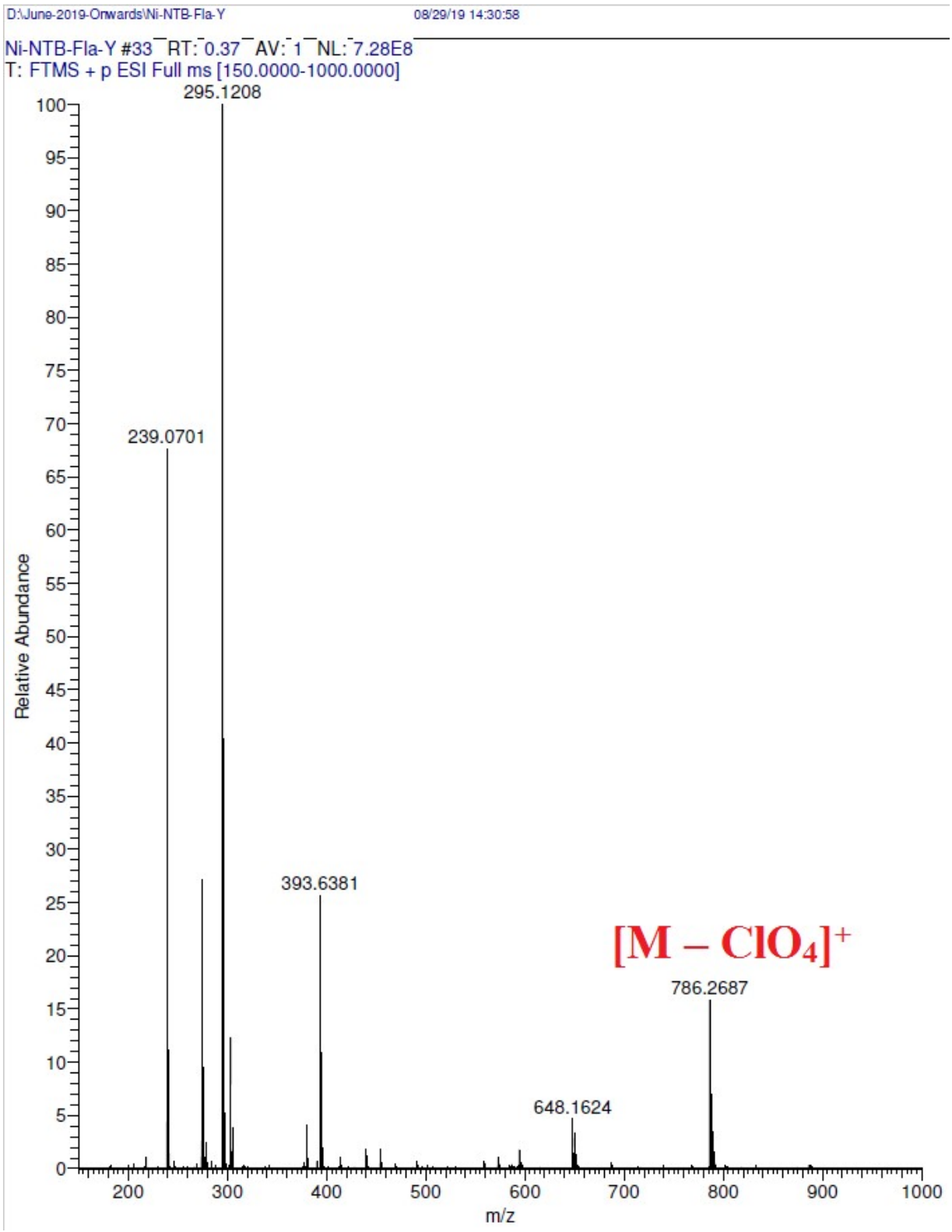

Figure S24. High Resolution Mass Spectra of [Ni(L3)(fla)]ClO_4 **3** in acetonitrile solution (1×10^{-3} M) at 25 ºC.

References

1. D. Jeong, S. Sun, D. Moon and J. Cho, *J. Inorg. Biochem.*, 2022, **226**, 111632.
2. T. Ajaykamal, M. Sharma, N. S. Islam and M. Palaniandavar, *Dalton Trans.*, 2021, **50**, 8045-8056.